

Nanoscale

Accepted Manuscript



This is an *Accepted Manuscript*, which has been through the Royal Society of Chemistry peer review process and has been accepted for publication.

Accepted Manuscripts are published online shortly after acceptance, before technical editing, formatting and proof reading. Using this free service, authors can make their results available to the community, in citable form, before we publish the edited article. We will replace this *Accepted Manuscript* with the edited and formatted *Advance Article* as soon as it is available.

You can find more information about *Accepted Manuscripts* in the [Information for Authors](#).

Please note that technical editing may introduce minor changes to the text and/or graphics, which may alter content. The journal's standard [Terms & Conditions](#) and the [Ethical guidelines](#) still apply. In no event shall the Royal Society of Chemistry be held responsible for any errors or omissions in this *Accepted Manuscript* or any consequences arising from the use of any information it contains.

Gain and Raman line-broadening with graphene coated diamond-shape nano-antennas

Charilaos Paraskevaïdis¹, Tevye Kuykendall², Mauro Melli², Alexander Weber-Bargioni², P. James Schuck², Adam Schwartzberg², Scott Dhuey², Stefano Cabrini² and Haim Grebel^{1}*

¹ *Electronic Imaging Center, NJIT, Newark, NJ 07102; grebel@njit.edu*

² *The Molecular Foundry, Lawrence Berkeley National Laboratory, Berkeley, CA 94720*

Abstract: Using Surface Enhanced Raman Scattering (SERS), we report on intensity-dependent broadening in graphene-deposited broad-band antennas. The antenna gain curve includes both the incident frequency and some of the scattered mode frequencies. By comparing antennas with various gaps and types (bow-tie vs diamond-shape antennas) we make the case that the line broadening did not originate from strain, thermal or surface potential. Strain, if present, further shifts and broadens those Raman lines that are included within the antenna gain curve.

I. Introduction

Surface enhanced Raman scattering (SERS) [1] is a major spectroscopic tool for efficient molecular identification down to the level of a few molecules [2-3]. In many SERS-based sensors, the molecules are adsorbed on a mesoscopic thin metal film [4-6] and the resultant optical scattering is detected far away from the film (far-field). Optimizing the scatterer's shape requires well-defined antenna structures [7-8]. The bandwidth of most SERS antennas is narrowly centered at the laser frequency; either because of particular antenna design, or, fabrication limitations. Narrow band antennas often provide gain to only the laser line and little or no gain to the Raman lines outside the antenna resonance curve. On the other hand, if the gain curve of narrow band antennas covers only the scattered Raman modes, then broadening and line red-shift are observed [9]. In near-field studies, antennas in a form of a tip are brought within a close proximity to the sample (tip enhanced Raman scattering, TERS [10-11]). Tip antennas are not broad band because they lack directivity, form travelling waves between substrate and antenna and allow multi local modes within the gap between the tip and the sample.

We concentrate on the electromagnetic effect [12]. In general, at low intensity, spontaneously scattered Raman signals linearly depend on the pump laser intensity with minimal line broadening, or peak shift [13]. A recent SERS study indicated that the intensity dependent Stokes signal for a test film at electronic resonance remains linear while the signal is within the electronic resonance and becomes nonlinear for frequencies outside that resonance range [14]. One may postulate that graphene,

which exhibits broadband loss [15] will also exhibit a linear response with respect to the laser intensity.

Raman signal amplification was attributed to the formation of surface plasmon/polariton modes in SERS antennas. This implies that high-order restoring fields may affect the Raman line's shape and width [16]. In addition, if both the pump and the scattered frequencies are plasmonic/polaritonic modes of a metallic resonator, then the transition rate between the two modes depends on their density of states (DOS); the DOS is substantially modified near metallic surfaces [17]. The modes' lifetime and, thereby our interpretation of the Raman line position and width depends on the DOS and loss of these resonator modes.

When experimental configurations are performed in the far-field, the SERS antenna has two roles: (a) maximizing absorption of the incident radiation laser mode for optimal incident-to-plasmon/polariton coupling and (b) enhancing the detection process by the geometrical antenna gain factor. This latter gain is the result of concentrating the otherwise uniformly emitted radiation into a well-defined solid angle. From such a point of view, one needs to maximize the overlapping integral of pump and probe signals [18]. Yet, *a priori*, it is not clear whether maximizing the overlap integral will lead to Raman line broadening.

II. The model

The transition probability for Stokes scatterings has two contributions: absorption and emission [19]. We use Fermi's Golden Rule: the rate of transition is $W_{fi}=(2\pi/\hbar^2) |H_{fi}|^2 \rho_f$ where H_{fi} is the transition matrix element between the pump and scattered modes and ρ_f

is the convoluted density of the final states (of both the phonons and scattered photons). For emission, $W_{fi}=B(\nu_S)\rho(\nu_S)(N_L+1)N_S$ and for absorption $W_{if}=B(\nu_L)\rho(\nu_L)(N_L+1)N_S$. $N_{S,L}$ are the number of photons in the resonator modes: S for Scatter and L for Laser. We can assume that $B(\nu_L)=B(\nu_S)=B$. The spontaneous cross-section is defined as $\sigma=(\lambda^2/8\pi)*P*Bg(\nu)\rho(\nu)$ where P is the occupation number of the phonon and $g(\nu)$ is the probability of finding a photon at frequency ν ($g(\nu)$ is also known as the gain curve distribution). We write:

$$\frac{dN_S}{dt} = N_0\sigma_S^{(0)}N_L(N_S + 1) - N_1\sigma_L^{(1)}N_S(N_L + 1) - N_S/\tau_S \quad (1a)$$

$$\frac{dN_L}{dt} = -N_0\sigma_S^{(0)}N_L(N_S + 1) + N_1\sigma_L^{(1)}N_S(N_L + 1) - N_L/\tau_L. \quad (1b)$$

Here $\sigma^{(0,1)}_{S,L}$ are the scattering cross sections with the superscript denoting the initial vibration state: either ground ($\nu=0$), or first excite ($\nu=1$) states. $N_{0,1}$ are the number of say, graphene atoms coating the resonator in either vibration state, $N_1/N_0 \sim \exp(-\hbar\Omega/k_B T)$ and $\Omega \approx \omega_L - \omega_S$ (the approximate equality is due to line-widths; in any event, $\Omega \ll \omega_L, \omega_S$). The last terms are losses suffered by the resonator modes and play a major role in mesoscopic films because of edge scatterings. Similar equations may be derived using an electromagnetic approach [20-22].

Thermal effects have two consequences: at high temperatures, the stimulated emission term, which is proportional to $N_L N_S (N_0 - N_1) = N_L N_S N_0 (1 - \exp(-\hbar\Omega/k_B T))$ decreases. High enough temperatures increase the phonon population at higher-order states leading to red-shifted peaks (unharmonicity effect – see below).

If the scattered mode is coupled to a resonator mode instead of free-space modes, then the Raman scattering rate increases by a factor of Q - the resonator quality

factor [17] - the density of states in free space, which is proportional to v_S^2/c_n^3 is now replaced by $\sim 1 \text{ mode}/(V \cdot \Delta v)$, with V the mode volume and $\Delta v = v/Q$ (this points to the attractiveness of nano-antennas for some applications). For cubic resonators the mode volume is $V \sim (\lambda_n/2)^3$. The mode volume for planar antennas made of gold is, $a^2 \cdot (\delta_d + \delta_m)$. The area of the antenna is, $a^2 \sim (\lambda_n/2)^2$ where, λ_n is the effective wavelength of the antenna's plasmonic modes (for dipole antennas, $a \sim \lambda_n/2$). The other dimensions are, $\delta_{d,m}$ - the $1/e$ decay-length in the dielectric and gold, respectively. For common dielectrics, $\delta_d \sim \lambda_d/2 \gg \delta_m$ and the density of states also scales as Q . Three additional factors add to the effectiveness of the process: (1) the increase in coupling efficiency between the incident laser radiation and the resonating antenna at v_L effectively increasing the antenna's cross section; (2) the increase in the coupling between the scattered wavelength and the resonating antenna at v_S and (3) the increase in detection efficiency: the radiated scattered modes at frequency v_S are directed more towards the normal to the antenna's axis (confocal arrangement) than isotropic. The latter is referred to as the antenna gain by the microwave community and it has a purely geometrical origin. For brevity, we refer to the entire amplification process by the antenna as gain.

Intensity-Dependent Line Broadening. When $N_L \gg N_S$, all terms proportional to N_S can be ignored and $dN_S/dt = -dN_L/dt$. One can assume exponential growth (or, exponential decay) and we write it as, $N_S/\tau_{\text{spont}} = -N_L/\tau_{\text{spont}}$ with the same time constant - they differ by their initial conditions ($N_S(t=0)=0$, $N_L(t=0)=N_{L0}=\text{const} \gg 1$). The time constant for spontaneous Raman scattering is $1/\tau_{\text{spont}} = p_0 B g(v) \rho(v)$. When we include the stimulated terms in 1b, the time constant of the plasmonic mode is modified by the gain coefficient $\gamma_S \sim N_L$: $1/\tau_S^{\text{eff}} \rightarrow 1/\tau_{\text{spont}}(1 + \gamma_S)$ and from 1a, $1/\tau_L^{\text{eff}} \rightarrow 1/\tau_{\text{spont}}(1 + \gamma_L)$ with

$\gamma_L \sim N_S$. The overall Raman line width is the sum, $\Delta\nu \sim 1/\tau_S^{\text{eff}} + 1/\tau_L^{\text{eff}}$. These modifications to the transition life-time may be explained by the induced emission and the induced absorption of the scattered plasmonic modes, respectively. The number of photons N_L is related to the laser mode intensity within the resonator by $N_L/V = I_L/c_n(\nu)/h\nu$ with $c_n(\nu_S)$ – the light phase velocity at ν_S . The effective life-time of the optical modes are related to their line width as $1/\tau \sim \Delta\nu$. The measurement of the natural vibration frequency width is thus impacted by the lifetime of the cavity plasmonic/polaritonic optical modes and the laser intensity. Discussion on the life-time of the vibration (phonon) mode is provided at the end of this paper.

III. Results

Diamond-shape antennas (D-ant) [23,24] exhibit a large bandwidth. The antenna exhibits a linear phase throughout its wide band resonance, as well [24]. From the discussion above, one would expect that the inclusion of scattered modes in the gain curve adds a higher degree of nonlinearity to the scattering process.

We chose graphene [25] as our test film. Current technology enables a uniform deposition of graphene, thus eliminating much of the uncertainty in its location and its concentration. Since it is thought that only a few local antenna regions contribute to the Raman amplification process, depositing graphene over the entire antenna should have a minimal impact on the overall detected signal at the far-field. Comparing scattering data from the antenna to scattering data from areas between the antennas provided us with a simple way to assess the amplification factor. Finally, graphene exhibits several Raman lines that can ‘map’ the gain region of the antenna.

Bow tie antennas [7] have been studied extensively for SERS applications, mainly because they exhibit a large 'hot spot' between the antennas' elements (Fig. 1b). Since a diamond antenna is just an inverted bow-tie structure, we used the acquired bow-tie data for comparison purposes. Figure 1a,b show typical near-field simulations of gain distribution for diamond shape (D-ant) at resonance and bow-tie antennas (BT-ant) at the D-ant's resonance. The gain (in dB) was defined as, $-10\log_{10}(|E_{\text{local}}|/|E_{\text{incident}}|)$. Accepted dispersion relations for suspended graphene, graphene on a substrate (alumina) and gold [26,27] were used. The conductivity of graphene, σ_0 , at high frequencies is constant and real, so one may write, $\varepsilon(\omega)=\varepsilon_b+i\sigma_0/\omega d$. We used $\varepsilon_b=5.8\varepsilon_0$ as the effective dielectric for graphene with a background material [28] and $d=3.38$ Angstroms for the effective graphene thickness. The scanning laser spot is much larger than the antenna and covers areas where graphene is partially situated on alumina - a separating layer between the gold antenna and the graphene - and partially suspended in air (due to the height of the antenna). We, therefore, write $\varepsilon_b^{(\text{eff})}=a_1\varepsilon_b^{(\text{alumina})}+a_2\varepsilon_b^{(\text{air})}$ with $a_1=0.1$ and $a_2=0.9$, the respective areas of antenna and air. The peak electric field intensity in the gap of the BT-ant is by far larger than the value for the D-ant (by more than 30 dB) and one may naively conclude that the BT-ant would be a superior amplifier (which is not the case here). The dominant factor for the far-field reflection spectra is the antenna shape (Figure 1c for rounded tip antennas with a gap of 12.4 nm). The spectral bandwidth of the D-ant is ca 50% wider than the BT-ant (see also white-light experiments in the SI section). The peak scattering wavelength shifts up as the antenna's height increases and shifts down as the gap becomes larger. Unlike BT-ant, 'hot spots' appear here at the antenna's

extremities. While the nominal dimensions of the D-ant and BT-ant were the same, the fabrication process could have unintentionally increased the gap of BT-ant by rounding their apices. If so, rounding of an antenna's tip increases the gap from ca 12 nm (for sharp tips) to 22 nm (with round tips) and therefore down-shifts its peak-resonance wavelength. The effect of lithographic rounding is less pronounced for the gap of D-ant: a gap increase by 2 nm may be expected. The results for BT-ant are consistent with previous results. Test films (or molecules in the antenna gap) may be viewed as providing coupling between the antenna's elements [29] and our finite-element simulations indicated that the graphene and alumina up-shift the antenna resonance wavelength by 10 nm. It also adds a small broadband absorption loss.

Figure 2a is a scanning electron microscope (SEM) image of our layout. Each antenna was surrounded by fiduciary marks, 2 μm away from the antenna. The rectangular patterns, oriented perpendicularly to one another, were used to examine the effect of two linearly orthogonal incident polarizations states. As shown by Figure 2c, the entire metal layout 'glowed' at scattering wavelengths when illuminated by a 633 nm HeNe laser, polarized along the antenna axis. Mostly the antennas were accentuated when pumped with a polarized 785 nm (Figure 2d). In this way, one can optically identify the antennas and marks at the scattered frequencies.

The spectral scattering background was substantially elevated at the antennas and necessitated correction. The spectra were fitted by a polynomial and subtracted from the data using two different routines to achieve similar results. A 800 cm^{-1} line may be observed 'riding' on that spectral background, as well (see also Fig. S7a in the SI section). We believe that amplification and broadening of the small 800 cm^{-1} line

(attributed to pure amorphous carbon [30], or graphitic edge [31]) overwhelmed the 500-1000 cm^{-1} spectral region. (The origin of the peak at 800 cm^{-1} is not quite settled. On one hand our data in the SI section clearly indicate a peak. At the same time, several authors [32,33] report on a broad band in that region. In principle, this extended band could overwhelm the data obtained with the antenna, yet did not quite appear in spectra obtained in-between them).

Images are shown in Figure 3 (see also the SI section) whose spectral background has been corrected. When the polarization of the pump 785 nm laser was made perpendicular to the antenna's axis, scatterings from one subset of the fiduciary marks became more pronounced (Figure 3c). The narrow side of the fiduciary marks (ca 100 nm) and disks (diameter 100 nm) are near scattering resonances and exhibited Raman data similar to the BT-ant.

The spatial profile of each Raman peak was fitted by a Gaussian distribution. The average spatial width at Raman frequencies (full width at half maximum, FWHM) was assessed as $1.06 \pm 0.02 \mu\text{m}$ for the D-ant, which is 1.4 times larger than the FWHM of the laser spot-size (assessed at $0.715 \mu\text{m}$ by a Gaussian beam approximation). This is also larger than the diffraction-limited scattered spot-size (assessed at $0.815 \mu\text{m}$ for the scattered wavelength of 895 nm). At scattered wavelengths, the cross section of the antenna became larger than the diffraction limited spot-size, which is typical of resonance conditions. Care was taken that the laser beam was in focus before and after scans; this conclusion was also based on observation from several scans over various regions). By comparison, the scan over the (rated) 10-nm gap BT-ant exhibited an antenna width of approximately 0.8 micron at the Raman G-line, only slightly larger

than the laser spot size but in accordance to the diffraction limited scattered mode. The scan of D-ant with perpendicular polarization exhibited effective antenna width of 0.9 ± 0.02 microns, alluding to its only partial resonance. The fact that BT-ant, situated on the same wafer not far from the D-ant, exhibited a near diffraction limited spot-size is in further proof that our system was well-aligned.

In Figure 4a,b we present as-is maps for the integrated graphene's 2D-line on 10-nm gap antennas. The D-ants are clearly visible (only two rows have been scanned) whereas the signals from fiduciary marks are much dimmer. Figure 4c shows uncorrected spectra for graphene on each antenna; the uncorrected curves include an elevated spectral background. After fitting, a large peak enhancement on the order of ca 100 times and a 5-fold peak broadening of the D-line were noted. Enhancement and broadening of the G-line was typically smaller: ca 10-fold enhancement and 3-fold broadening. The 2D-line was broadened by a factor of ca 1.5 with little enhancement. The largest identifiable enhancement and line broadening was observed for the D graphene line - closer to the resonance peak. The smaller enhancement and broadening was detected for the 2D graphene line – furthest from the resonance peak. This was as if the antenna gain curve was superimposed on the Raman scattering spectra. Furthermore, 30-nm gap antennas exhibited a large line broadening to only the D-line and no broadening and little amplification to all other Raman lines. As the antenna's gap increases, its center resonance wavelength is shifted towards the shorter wavelengths hence covering fewer Raman lines.

Fig. 4d shows 2D-lines for the D- and BT-ant. The G- and D-lines of the D-ant were further down-shifted with respect to the corresponding BT-ant: the G-line was

down-shifted by 21 cm^{-1} and the D-line was down-shifted by 10 cm^{-1} . There is a notable broadening of these lines for graphene on the D-ant. *If built-in strain has equally affected the 2D-line of both the D- and BT-ant, then the difference between the two spectra ought to be attributed to the difference in their related antenna gain (peak resonance wavelength and bandwidth).*

Besides an obvious enhancement and substantial broadening of the D and the 2D lines, the D-ants exhibited bandpass characteristics between the cut-off filter and ca 1700 cm^{-1} . In contrast, the BT-ant exhibited a monotonic tail away from the laser line. The height of this tail varied, yet, an increased tail height did not lend itself to larger Raman signals and sometimes to the contrary. The monotonous tail was also characteristic of fiduciary marks and could be used to distinguish resonating and partly resonating structures. The monotonous tail on the fiduciary marks for the 633 nm laser is a bit puzzling. A HeNe laser has a very narrow line width, which may be eliminated rather effectively by a cut-off filter, placed in front of the detector array. This could suggest the existence of a broader line, perhaps due to photoluminescence of our 17 nm thick gold layer [34].

Figure 5 shows a spatial scan over the graphene coated antenna in 200 nm steps. The intensity profile of the 785 nm laser spot is Gaussian (as judged by the interference pattern of the spot through a pin-hole – not shown); therefore, the spatial scan may be translated into an intensity scan. The evolution of the spectra is shown in Figure 5a. Three of these spectra are shown in Figure 5b. Specifically, the spectra were taken at the beginning, middle and at the end of the spatial scan. The start and end points were separated by 1.8 microns with an estimated 10% of the maximal laser

intensity on each. Figure 5b was normalized to the peak D-line amplitude because the scan points were not symmetrically dispersed about the antenna's position. The broadening and narrowing of the G-line is significant because the line is less likely to be sensitive to the presence of defects as the D-line. Since the measured Raman signal is sum of contributions from the area around and on the antenna, damaged graphene if exists, will affect the linewidth at the end of the spatial scan.

IV. Discussions

Accumulated data are provided in Table 1. Strained samples exhibited shifts to both the 2D and G-lines. Un-strained samples were identified by little shift to their 2D-line and, yet, a shift to their G-line. Overall, there is a sizeable amplification and broadening to the D line, little amplification and broadening to the 2D-line and an apparent amplification and broadening to the G-line. The case for intensity-dependent broadening is made below.

Intensity-dependent line broadening could be attributed to several factors and we will comment on each one.

(a) Amorphous carbon. The argument for it goes as follows: amorphous carbon was formed at the antenna's tips through photo- or thermal-carbonation [35,36] due to extremely large electric fields [37]. Accordingly, its Raman lines overwhelmed the scattering signals. To counter this argument we first point that the 'hot spot' model predicts that only a few graphene atoms are involved in SERS. If so, the line shift and broadening allude to temperatures in the hundreds of degrees range [38]. At those temperatures, the spots ought to be long burnt out since the experiments were

conducted in open atmosphere. As a result, the measured signal should have been attributed to only plain graphene surrounding the burnt spots and the antenna gain should have been dropped to unity, which is not the case here (see Figures 6,7). The persistent scans over the antennas and the single scan of Figure 5 should have resulted in a 'damaged' spectra, which did not happen. Secondly, line broadening and peak shift occurred for the G and 2D lines as well. This means that the effect cannot be simply attributed to developing defects (which mostly affect the D-line and indirectly, decreases the intensity of the 2D line).

(b) Thermal effects. Obvious concerns are thermal effects. An apparent peak shift of ca 2% observed for some of the D-ant may be consistent with anharmonicity [38]. Anharmonicity results from volumetric change of the vibration oscillator. Yet, a 2% down peak-shift is equivalent of thermal heating by a few hundreds of degrees. This conclusion may also be derived if we assume that the line width is proportional to $k_B T$: broadening by a factor of 5 or even 3 translates to a temperature change of several hundreds of degrees, as well. Our experience with graphene at those temperatures in open air is that the graphene oxidizes and burns, which did not happen to our films.

(c) Laser post-annealing. While creating damage, the laser annealed the graphene thereby giving the appearance of broad peaks. For one, the effect we measured was repetitive (namely, reversible). Secondly, laser annealing should have blue-shifted the graphene Raman lines [39], contrary to our present data.

(d) Stress and strain. Compressive stress results in blue shifted peaks. Strain, or tensile stress will red-shift the peaks to lower wavenumbers [40]. Built-in strain, such as arising from fabrication methods, should shift all Raman lines [41] and ought to show

up with both the 633 nm, 532 and 785 nm lasers regardless of resonance conditions [42-46]. Strain splits both the G- and 2D-lines and one could argue that broadening could be the result of poor line resolution. Moreover, the strain could be larger on the antenna due to its height. Unresolved G-line peak on the antennas means that the strain was less than 0.3% with an averaged peak-shift of less than -7 cm^{-1} [45]. At the same time, since the ratio of peak shifts is, $\Delta w_{2D}^{(\epsilon)}/\Delta w_G^{(\epsilon)} \sim 2.2$ [44] unresolved peak split will be exhibited as a broadened 2D-line, which would also be shifted by more than 15 cm^{-1} . These arguments are not supported by data in Table 1 (e.g., D_10_03 where the G-line is much broader than the 2D-line).

In Figs S9 in the SI section we present the 2D line of two antennas under various excitation conditions. One antenna clearly exhibited a red-shifted 2D line, which may attributed to strain in addition to intensity-dependent line broadening. The other antenna did not exhibit any intensity dependent shift or line-broadening to its 2D line, similarly to Fig. 7 below. The line-width of the shifted 2D-line was more sensitive to the laser intensity than the un-shifted one (Fig. S9a). Overall, strain alone cannot explain the intensity-dependent line broadening of the D and G lines.

In addition, Fig. S4c for perpendicular polarization clearly exhibits no shift and no broadening to the 2D-line. This could mean that a uniaxial strain acts along the antenna's axis (and therefore un-detected for perpendicularly polarized beam). At the same time, the D and G-exhibited small shift and *large* broadening, which is not consistent with the effect of uniaxial strain. Therefore, for those antennas that did not exhibit strain, line shift and broadening should be attributed to frequency pulling and gain of the resonator.

(e) Substrate effects and built-in surface potential. Substrates and surface potential at the interface between substrate and layer may affect the Raman peak position, which in principle, could lead to Raman line broadening [46-51]. The combined effects of strain and doping may result in a line, which is partially red-shifted and partially blue-shifted [46]. In the SI section we argue that a larger shift to the G-line with respect to the 2D-line (Table 1) is not consistent with this scenario. Specifically, the stress will always overwhelm the doping effect and the net result would be a larger shift to the 2D-line than the G-line. Shifts to the Fermi energy below, say ± 100 meV, little affect the 2D-line but it will blue-shift it nonetheless. This is not what we observed here.

Our gold antennas are separated from the graphene by an insulator layer (alumina), minimizing a direct electronic doping of the graphene (also known as the chemical effect [12]). Yet, some of the photo-induced carriers in the gold may tunnel or be trapped with time-constants on the order of ps. In the Si section we make the case that optical doping would shift the Fermi energy by only 3 meV. The relatively small value is due to the small area of the antenna with respect to the laser spot size and the relatively low metal loss at that wavelength range.

(f) The case for Intensity-dependent line broadening. We selected antennas that did not exhibit a 2D-line shift. The data are shown in Figure 6 and 7 upon ramping-up and down the laser intensity through $I_L=5.14, 16.1$ and 28.4 mW. The 2D-line suffered from low detector responsivity; nevertheless, its scattering signal depended on the pump laser intensity. We define the amplitude gain, g , as, $I_{ant}/I_{ref} = I_L g$, where I_{ant} - the signal on the antenna (including its surroundings) and I_{ref} - the signal measured in-

between antennas. The total scattered signal when the laser spot resides on the antenna is $I_{\text{ant}}=aI_L+rI_L$ because the antenna occupies only a small fraction of the entire laser spot. For spontaneous Raman scattering, the coefficients a (for antenna) and r (for the reference) are constant of the laser intensity, I_L . If the reference signal in-between the antennas is available (Figure 6a), then $I_{\text{ant}}/I_{\text{ref}}=I_L(1+r/a)\equiv I_Lg$. The gain coefficient g is constant of intensity for spontaneous Raman scattering as may be implied by Figure 6b for the G- and 2D lines. If signal for the antenna's surroundings is not available, either because it is too weak, or suffers from too much noise, one may plot the peak amplitude and its integrated peak value as a function of the laser intensity (Figure 6c,d). If both plots are linear, then the coefficient $g(I_L)$ is constant, again as may be implied for the G- and D-lines. If the graphene on the antenna apices was progressively damaged upon an increase of the laser intensity, then the curve for the D line (mostly affected by the damage) would have the largest gain value at the lowest incident laser power. At the largest laser power, the signal would mostly come from the remaining non-damaged areas and would approach unity; in contrast to Figure 6b.

In Figure 7 we show spectral curves for an area which was first scanned at the highest intensity, $I_L=28.4$ mW. As the laser intensity was reduced by a factor of ~ 3 (16.1 mW/5.14 mW) the integrated D-line signal has reduced by a factor of 5.7 indicating that both the amplitude and the line width have been affected. Similarly, the G-line and the 2D lines exhibited reduction of almost 3 and 5 in their respective integrated signals. Due to the relatively large laser spot size and a small step size, each antenna was scanned at least four times with parallel and perpendicular polarization states (with respect to the antenna axis). The order of the scans varied with

no obvious lingering effect. If the graphene was damaged during previous scans, the scattering amplitude would decrease but not its line width. A scan with a 532 nm laser at 1 mW (Fig S1b in the SI section) was made after completing the intensity scans. No apparent damage was noted as judged by a small D-line.

Intensity-dependent gain implies coherent effects. It is interesting to note that the dimension of our antennas are well within the dimension of the equivalent plasmonic/polaritonic wavelength for the graphene, which is in the IR region [50-55]. While spontaneous Raman scattering for graphene is not expected to couple to a propagating surface modes, it has been shown that higher-order nonlinear effects could provide such coupling [56]. Detailed analysis of this process is beyond the scope of this paper.

Finally, an equation for the excited phonon state, N_1 may be written as,

$$\frac{dN_1}{dt} = N_0\sigma_S^{(0)}N_L(N_S + 1) - N_1\sigma_L^{(1)}N_S(N_L + 1) - N_1/\tau_1. \quad (1c)$$

Here, the life-time of the phonon at the excited state τ_1 includes all processes, such as electron-phonon and phonon-phonon interactions [57]. Indirectly, the cavity gain affects the time-constant of the excited phonon too: $1/\tau_1^{\text{eff}} \rightarrow 1/\tau_1(1+\gamma_1^{(\text{pn})})$ with $\gamma_1^{(\text{pn})} \sim N_S N_L$.

V. Conclusions

We demonstrated frequency selective Raman signal enhancement and line broadening with graphene-coated diamond-shape nano-antennas. Selective line broadening was also correlated with the antenna gap (which dictates the antenna resonance wavelength and hence the coverage of Raman lines by the antenna gain curve). Intensity

dependent gain, line broadening and peak-shift were attributed to plasmonic/polaritonic modes in these nano-optical amplifiers.

Acknowledgment: we thank E. Wood from the molecular Foundry at LBL for technical support. Portion of this work were performed as a user project at the Molecular Foundry, supported by the Office of Science, Office of Basic Energy Sciences, of the U.S. Department of Energy under Contract No. DE-AC02-05CH11231.

Table 1: accumulated data

Sample	line-shift/line-width/amplitude	line-width/amplitude	line-shift/line-width/amplitude	line-width/amplitude
strained	D_10_03 ⁽¹⁾	Reference_10 ⁽¹⁾	D_30_09 ⁽³⁾	Reference_30 ⁽³⁾
D-line	-13/203/274	55/6	+13/170/34	26/11
G-line	-30/90/171	35/21	-2/35/56	30/41
2D-line	-23/56/19	34/7	-11/57/20	52/20
un-strained	D_10_07 ⁽²⁾	Reference_10 ⁽²⁾	D_10_03 ⁽⁴⁾	Reference_10 ⁽⁴⁾
D-line	NA/141/58	NA	+12/179/120	124/6
G-line	-8/21/161	12/32	-20/73/98	35/35
2D-line	+4/36/26	31/20	-2/44/19	42/15

Shifts and line-width are denoted in cm^{-1} . Line shifts are noted with respect to data in-between antennas (Reference). Amplitudes are provided in counts. Errors varies but were ca $\pm 4 \text{ cm}^{-1}$. For 785 nm laser, the 2D line for the reference appeared mostly at 2601 cm^{-1} (and with some exceptions at 2607 cm^{-1}), the G-line mostly at 1587 cm^{-1} , and the D line at 1298 cm^{-1} (and with some exceptions at 1304 cm^{-1}). The laser polarization was parallel to the antenna axis except in (4). The position of the D-line is subjected to a larger error due to its larger width.

- (1) Figure 4 D-ant with a 10 nm gap at 28.4 mW; the laser polarization was parallel to the antennas' axis
- (2) Figure 7a D-ant with 10 nm gap at 16.1 mW; the laser polarization was parallel to the antennas' axis
- (3) Figure S6b D-ant with a 30 nm gap at 28.4 mW;
- (4) Figure S4c D-ant with a 10 nm gap at 28.4 mw with the laser polarization perpendicular to the antenna axis.

References

- [1] M. Fleischmann, P. J. Hendra, A. J. McQuillan, "Raman spectra of pyridine adsorbed at a silver electrode", *Chem. Phys. Letters*, 26, 163-166 (1974).
- [2] S. Nie and S. R. Emory, "Probing Single Molecules and Single Nanoparticles by Surface-Enhanced Raman-Scattering", *Science*, 275, 1102-1105 (1997).
- [3] K. Kneipp et al, "Single Molecule Detection using Surface-Enhanced Raman Scattering", *Phys. Rev. Letts*, 78, 1667-1671 (1997).
- [4] Katherine A. Willets and Richard P. Van Duyne, "Localized Surface Plasmon Resonance Spectroscopy and Sensing Annual Review of Physical Chemistry, 58, 267-297 (2007) DOI: 10.1146/annurev.physchem.58.032806.104607
- [5] Jon A. Schuller, Edward S. Barnard, Wenshan Cai, Young Chul Jun, Justin S. White and Mark I. Brongersma, "Plasmonics for extreme light concentration and manipulation", *Nature Materials*, 9, 193-204 (2010). DOI: 10.1038/nmat2630.
- [6] Weigao Xu, Xi Ling, Jiaqi Xiao, Mildred S. Dresselhaus, Jing Kong, Hongxing Xu, Zhongfan Liu, and Jin Zhang, "Surface enhanced Raman spectroscopy on a flat graphene surface", *PNAS*, 109, 9281-9286 (2012).
- [7] P. J. Schuck, D. P. Fromm, A. Sundaramurthy, G. S. Kino, and W. E. Moerner, "Improving the Mismatch between Light and Nanoscale Objects with Gold Bowtie Nanoantennas", *Phys. Rev. Lett.*, 94 (1), 017402-4 (2005).
- [8] P. Alonso-González, P. Albella, M. Schnell, J. Chen, F. Huth, A. García-Etxarri, F. Casanova, F. Golmar, L. Arzubaga, L.E. Hueso, J. Aizpurua and R. Hillenbrand, "Resolving the electromagnetic mechanism of surface-enhanced

- light scattering at single hot spots”, *Nat. Comm.* 3, 684 (2012). [Dol: 10.1038/ncomms1674](https://doi.org/10.1038/ncomms1674).
- [9] Behnood G. Ghamsari, Anthony Olivieri, Fabio Variola, and Pierre Berini, "Frequency pulling and line-shape broadening in graphene Raman spectra by resonant Stokes surface plasmon polaritons", *PHYSICAL REVIEW B*, 91, 201408(R) (2015).
- [10] Raoul M. Stockle, Yung Doug Suh, Volker Deckert and Renato Zenobi, "Nanoscale chemical analysis by tip-enhanced Raman spectroscopy", *Chem Phys. Letts*, 318, 131–136 (2000).
- [11] Dmitri K. Gramotnev and Sergey I. Bozhevolnyi, "Nanofocusing of electromagnetic radiation", *Nature Photonics*, 8, 13–22 (2014) [doi:10.1038/nphoton.2013.232](https://doi.org/10.1038/nphoton.2013.232)
- [12] Saikin, S. K., Chu, Y., Rappoport, D., Crozier, K. B. & Aspuru-Guzik, A. Separation of electromagnetic and chemical contributions to surface-enhanced Raman spectra on nanoengineered plasmonic substrates. *J. Phys. Chem. Lett.*, 1, 2740–2746 (2010).
- [13] A. Yariv, *Quantum Electronics*, J. Wiley and Sons, 1989 p 462-473.
- [14] M Baibarac, I Baltog, L Mihut, A Matea and S Lefrant, "Nonlinear features of surface-enhanced Raman scattering revealed under non-resonant and resonant optical excitation", *J. Opt.*, 16035003 (2014). [doi:10.1088/2040-8978/16/3/035003](https://doi.org/10.1088/2040-8978/16/3/035003).

- [15] Kin Fai Mak, Long Ju, Feng Wang, Tony F. Heinz, "Optical spectroscopy of graphene: From the far infrared to the ultraviolet", *Solid State Communications*, 152, 1341–1349 (2012)
- [16] H. Grebel, "Are large local fields necessary for the observation of Surface Enhanced Raman Scattering?", NLO, OSA Topical Meeting, abstract WC4, (2004).
- [17] E. M. Purcell "Spontaneous emission probabilities at radio frequencies" *Phys. Rev.*, 69, 681 (1946)
- [18] Francisco J. Lopez, Jerome K. Hyun, Uri Givan, In Soo Kim, Aaron L. Holsteen, and Lincoln J. Lauhon, "Diameter and Polarization-Dependent Raman Scattering Intensities of Semiconductor Nanowires", *Nano Lett.* 12(5), 2266–2271 (2012).
- [19] R. Hellwarth, "Theory of Stimulated Raman Scattering", *Phys. Rev. Letts.*, 130, 1850-1852 (1963).
- [20] Xiaodong Yang and Chee Wei Wong, "Coupled-mode theory for stimulated Raman scattering in high-Q/Vm silicon photonic band gap defect cavity lasers ", *Opt. Exp.* 15, 4763-4780 (2007).
- [21] X. Checoury, Z. Han, M. El Kurdi, and P. Boucaud, "Deterministic measurement of the Purcell factor in microcavities through Raman emission", *Phys. Rev. A* 81, 033832 (2010)
- [22] Benjamin Petrak, Nicholas Djeu, and Andreas Muller, "Purcell-enhanced Raman scattering from atmospheric gases in a high-finesse microcavity", *Phys. Rev. A* 89, 023811 (2014).
- [23] E. Bruce, Directive antenna, US Patent 2,282,565 (1942)

- [24] Nan Ni and H. Grebel, "2-element Independently Center-Fed Dipole Array for Ultra-Wideband and Ultra-Short Pulse Applications", *IEEE Antennas and Wireless Propagation Letters* **5** (4), pp. 127-129 (2006).
- [25] A. K. Geim, "Graphene: Status and Prospects", *Science*, **324** (5934), 1530-1534 (2009): DOI: 10.1126/science.1158877.
- [26] L.A. Falkovsky, "Optical properties of graphene", *Journal of Physics: Conference Series* **129**, 012004 (2008).
- [27] P. B. Johnson, R. W. Christy, "Optical Constants of the Noble Metals", *Phys. Rev. B* **6**, 4370–4379 (1972).
- [28] E. H. Hwang and S. Das Sarma, "Dielectric function, screening, and plasmons in 2D graphene", <http://arxiv.org/abs/cond-mat/0610561v3>.
- [29] H. Grebel, "Surface Enhanced Raman Scattering - phenomenological approach", *J. Opt. Soc. Am. B*, **21**, 429-435 (2004).
- [30] M. A. Tamor and W. C. Vasell, "Raman fingerprinting of amorphous carbon films", *J. Appl. Phys.*, **76**, 3823-3830 (1994).
- [31] PingHeng Tan, Svetlana Dimovski and Yury Gogotsi, "Raman scattering of non-planar graphite: arched edges, polyhedral crystals, whiskers and cones", *Phil. Trans. R. Soc. Lond. A*, (2004). 10.1098/rsta.2004.1442
- [32] A.C. Ferrari, J. Robertson, "Resonant Raman spectroscopy of disordered, amorphous, and diamondlike carbon", *Phys. Rev B* **64**, 075414 (2001).
- [33] F. Li, J.S. Lannin, "Disorder induced Raman scattering of nanocrystalline carbon", *Appl. Phys. Lett* **61**, 2116-2118 (1992). doi: 10.1063/1.108324.

- [34] Helen Armstrong, D. P. Halliday, Damian P. Hampshire, “Photoluminescence of gold, copper and niobium as a function of temperature”, *Journal of Luminescence* 129 1610–1614 (2009).
- [35] A. C. Ferrari and J. Robertson, “Raman spectroscopy of amorphous, nanostructured, diamond-like carbon, and nanodiamond”, *Phil. Trans. R. Soc. Lond. A* 362, 2477–2512 (2004).
- [36] L. G. Cancado, A. Jorio, E. H. Martins Ferreira, F. Stavale, C. A. Achete, R. B. Capaz, M. V. O. Moutinho, A. Lombardo, T. S. Kulmala, and A. C. Ferrari, “Quantifying Defects in Graphene via Raman Spectroscopy at Different Excitation Energies”, *Nano Lett.* 11, 3190–3196 (2011).
[dx.doi.org/10.1021/nl201432g](https://doi.org/10.1021/nl201432g)
- [37] Fred Schedin, Elefterios Lidorikis, Antonio Lombardo, Vasyl G. Kravets, Andre K. Geim, Alexander N. Grigorenko, Kostya S. Novoselov, and Andrea C. Ferrari, “Surface-Enhanced Raman Spectroscopy of Graphene”, *ACS Nano*, 4(10), 5617–5626 (2010).
- [38] Guy Lucazeau, “Effect of pressure and temperature on Raman spectra of solids: anharmonicity”, *J. Raman Spectrosc.* 34, 478–496 (2003).
- [39] L.M. Malarda, M.A. Pimentaa, G. Dresselhaus, M.S. Dresselhaus, “Raman spectroscopy in graphene” *Physics Reports* 473, 51–87 (2009).
- [40] Yan Zhang, Zafar Iqbal, Sankaran Vijayalakshmi, and Haim Grebel, “Stable hexagonal-wurtzite silicon phase by laser ablation”, *Appl. Phys. Letts*, 75, 2758-2760 (1999).

- [41] Sebastian Heeg, Roberto Fernandez-Garcia, Antonios Oikonomou, Fred Schedin, Rohit Narula, Stefan A. Maier, Aravind Vijayaraghavan, and Stephanie Reich, "Polarized Plasmonic Enhancement by Au Nanostructures Probed through Raman Scattering of Suspended Graphene", *Nano Letts*, 13, 301-308 (2013).
- [42] B. V. Kamenev, H. Grebel, T. I. Kamins, R. Stanley Williams, J. M. Baribeau, D. J. Lockwood and L. Tsybeskov, "Polarized Raman scattering and localized embedded strain in self-organized Si/Ge nanostructures", *Appl. Phys. Letts*, 83, 5035-5038 (2003).
- [43] T. M. G. Muhiuddin et al, "Uniaxial axial strain in graphene by Raman spectroscopy: G peak splitting, Gruneisen parameters and sample orientation", *Phys. Rev B* 79 205433 (2009).
- [44] Duhee Yoon, Young-Woo Son and Hyeonsik Cheong, "Strain-Dependent Splitting of the Double-Resonance Raman Scattering Band in Graphene", *PRL* 106, 155502 (2011)
- [45] Mark A. Bissett, Masaharu Tsuji and Hiroki Ago, "Strain engineering the properties of graphene and other two-dimensional crystals", *Phys.Chem.Chem.Phys.*, 16, 11124 (2014).
- [46] Ji Eun Lee, Gwanghyun Ahn, Jihye Shim, Young Sik Lee & Sunmin Ryu, "Optical separation of mechanical strain from charge doping in graphene" *Nat Comm.* 3:1024, (20). DOI: 10.1038/ncomms2022.

- [47] Andrea C. Ferrari, " Raman spectroscopy of graphene and graphite: Disorder, electron–phonon coupling, doping and nonadiabatic effects", *Solid State Communications* 143, 47–57 (2007). doi:10.1016/j.ssc.2007.03.052
- [48] Dong Su Lee, Christian Riedl, Benjamin Krauss, Klaus von Klitzing, Ulrich Starke, and Jurgen H. Smet, "Raman Spectra of Epitaxial Graphene on SiC and of Epitaxial Graphene Transferred to SiO₂", *Nano Lett.*, 8, 4320-4325 (2008).
- [49] Yumeng Shi, Xiaochen Dong, Peng Chen, Junling Wang, and Lain-Jong Li, "Effective doping of single-layer graphene from underlying SiO₂ substrates", *Phys. Rev. B* 79, 115402 (2009).
- [50] J. M. Caridad, F. Rossella, V. Bellani, M. Maicas, M. Patrini, and E. Díez, "Effects of particle contamination and substrate interaction on the Raman response of unintentionally doped graphene", *J. Appl. Phys.* 108, 084321 (2010).
- [51] Guillaume Froehlicher and Stéphanie Berciaud, "Raman spectroscopy of electrochemically gated graphene transistors: Geometrical capacitance, electron-phonon, electron-electron, and electron-defect scattering", *Phys. Rev. B*, 91, 205413 (2015)
- [51] Marinko Jablan, Hrvoje Buljan, and Marin Soljačić, "Plasmonics in graphene at infrared frequencies", *Phys. Rev. B* 79, 115402 (2009).
- [52] Frank H. L. Koppens, Darrick E. Chang, and F. Javier García de Abajo, "Graphene Plasmonics: A Platform for Strong Light-Matter Interactions", *Nano Lett.* 11, 3370–3377 (2011).
- [53] Z. Fei, A. S. Rodin, G. O. Andreev, W. Bao, A. S. McLeod, M. Wagner, L. M. Zhang, Z. Zhao, M. Thiemens, G. Dominguez, M. M. Fogler, A. H. Castro Neto,

- C. N. Lau, F. Keilmann & D. N. Basov, "Gate-tuning of graphene plasmons revealed by infrared nano-imaging", *Nature*, 487, 82–85 (2012)
doi:10.1038/nature11253
- [54] A. N. Grigorenko, M. Polini and K. S. Novoselov, "Graphene plasmonics", *Nature Phot.*, 6, 749 (2012).
- [55] Tony Low and Phaedon Avouris, "Graphene Plasmonics for Terahertz to Mid-Infrared Applications", *ACS Nano*, 8, 1086–1101 (2014).
- [56] Amrita Banerjee and Haim Grebel, "Nonlinear behavior of vibrating molecules on suspended graphene waveguides", *Optics Letters*, 38(2), 226–228 (2013).
- [57] Andrea Tomadin, Daniele Brida, Giulio Cerullo, Andrea C. Ferrari, and Marco Polini, "Nonequilibrium dynamics of photoexcited electrons in graphene: Collinear scattering, Auger processes, and the impact of screening", *Phys. Rev. B*, 88, 035430 (2013)

Figure Captions

Figure 1: Near-field and far-field patterns. Near-field and far-field patterns. Near-field gain distribution in decibels (dB) for (a) diamond antenna (D-ant) at resonance and, (b) bow-tie antenna (BT-ant) evaluated at the resonance frequency of the D-ant. The gain is defined as, $-10\log_{10}(|E_{\text{local}}|/E_{\text{incident}})$. The simulations were conducted with the full structure as described in the Method section (namely, including the alumina and graphene layers). (c) Normalized far-field reflection distribution. The two solid lines are for rounded tips at a 12.4 nm gap. Simulations for rounded BT-ant with a 22 nm gap are shown by the dash curve.

Figure 2: Electronic and optical scattering images. (a) SEM image of the layout: the yellow arrows point to the position of antennas; the light blue arrows point to the position of marks. (b) Diamond-shape optical antenna (D-ant). (c) As-is image for the integrated G-line when the sample was illuminated by a polarized 633 nm HeNe laser. Laser polarization was along the antenna axis (the x-axis). (d) As-is image for the integrated G-line when the sample was illuminated with a 785 nm laser. The laser polarization was along the antenna axis.

Figure 3: Spatial maps with spectral background corrected. (a) Integrated graphene D-line. (b) Integrated graphene G-line. Both **a**, and **b**, were taken with laser polarization parallel to the antenna's axis. (c) Integrated graphene D-line taken with laser polarization perpendicular to the

antenna's axis. A slight shift of the stage is noted. The antenna's gap of D-ant was nominally 10 nm and the layout was illuminated by a $\lambda=785$ nm laser.

Figure 4: Spatial maps and Raman spectra. (a) As-is spatial maps of graphene 2D line taken with (a) BT-ant and (b) with D-ant. The laser wavelength was 785 nm polarized along the antenna's axis and the antenna's gap was nominally 10 nm. Yellow arrows point to the antennas; light blue arrows point to the fiduciary marks. An optical filter cuts the laser line near zero for both antennas. (c) As-is Raman spectra of both antenna types. (d) Raman spectra. The spectral background was subtracted. The inset shows a typical spectrum of graphene between the D-ant; the relative small amplitude of the 2D-line is due to the limited sensitivity of the Si detector array in this spectral range (~ 980 nm; see also data for 633 nm laser in the SI section)

Figure 5. Spatial scans and Raman spectra. (a) Spectral data while the focused laser spot of ca 715 nm was scanning the ca 150 nm D-ant in steps of 200 nm. The spectral range was $1000-3000$ cm^{-1} . The laser intensity was maximal, 28.4 mW. The inset exhibits the same data in reverse order. (b) Three raw spectral data of graphene on D-ant: scans 5 (green solid circles), 8 (red solid circles) and 14 (blue open circles). Scan 8 was at maximal power. Scans 5 and 14 were separated by 1.8 μm at 10% of maximal laser power. The signals were normalized to the peak amplitude of the D-line.

Figure 6. Amplitude and integrated gain. (a) The signal in-between antennas exhibits a linear dependence on the laser intensity (spontaneous Raman scattering). The largest signal comes from the G-line; the largest intensity-dependent effect was obtained for the D-line. (b) Amplitude Gain, defined as the ratio between the signal on the antenna and the signal obtained for area between the antennas, as a function of laser intensity. Alternatively, one may plot the peak amplitude (c) and the integrated peak amplitude (d) as a function of the laser intensity. The set of antennas is different than the one shown in (a), (b).

Figure 7. Intensity-dependent spectra. Fitted spectra of D-ant taken at (a) $I_L=16.1$ mW and followed by (b) $I_L=5.14$ mW. The widths of the D-, G- and 2D-lines were, respectively: (a) 140 ± 3 , 21 ± 1 , 36 ± 3 cm^{-1} on the antennas and 12 ± 2 , 31 ± 3.5 cm^{-1} for the area between them (there was no observable D-line). (b) 74 ± 4 , 17 ± 1 , 37 ± 4.5 cm^{-1} on the antennas and 11 ± 2 , 25 ± 2.5 cm^{-1} for the area between them. Upon a decrease of the laser intensity by approximately a factor of 3, the decrease in the integrated peak count was, 5.7, 3 and 5 for the D-, G- and 2D-lines, respectively. The slightly lower 2D line in (b) compared to (a) might be the result of a smaller signal to noise ratio.

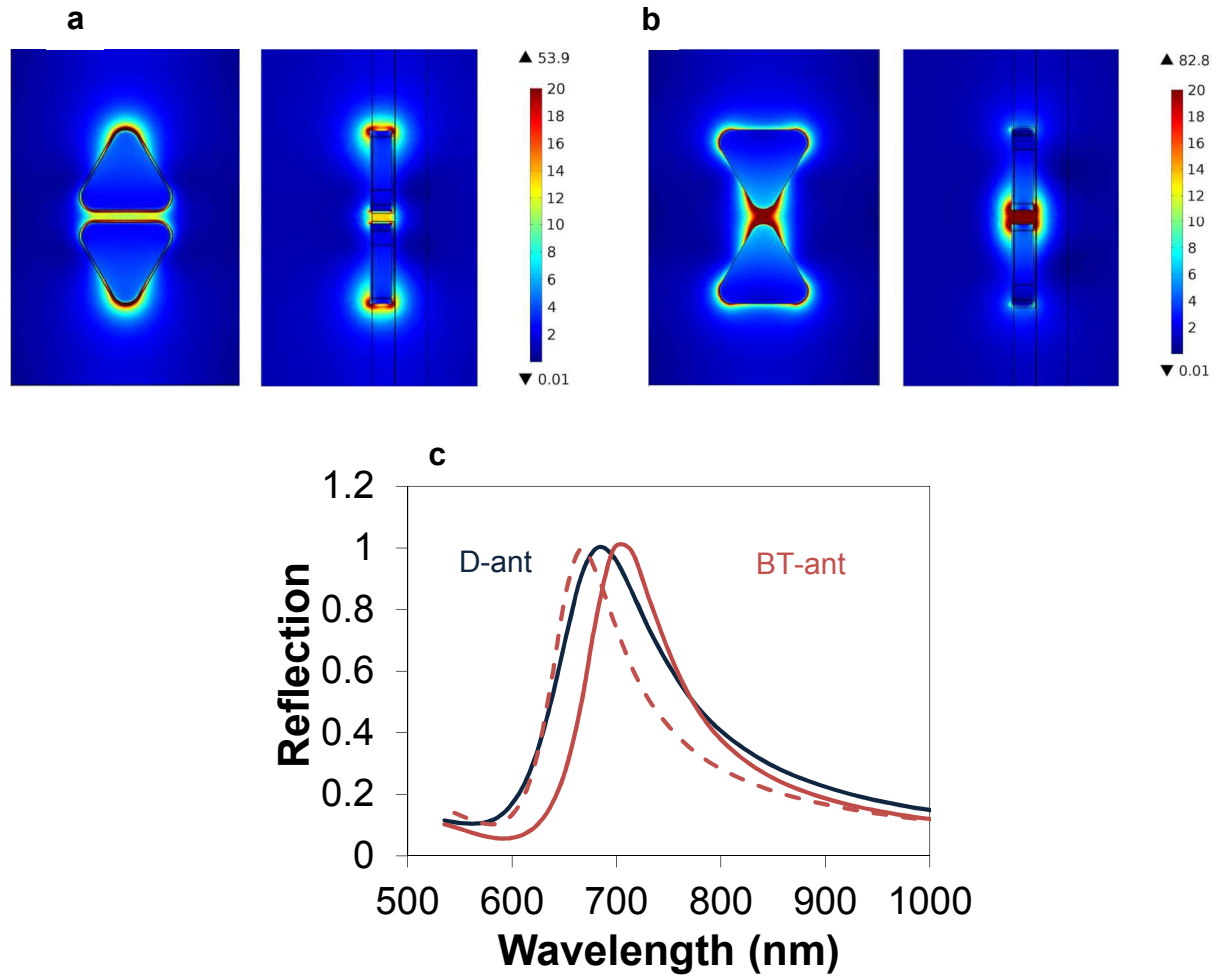


Figure 1: Near-field and far-field patterns. Near-field gain distribution in decibels (dB) for (a) diamond antenna (D-ant) at resonance and, (b) bow-tie antenna (BT-ant) evaluated at the resonance frequency of the D-ant. The gain is defined as, $-10\log_{10}(|E_{\text{local}}|/|E_{\text{incident}}|)$. The simulations were conducted with the full structure as described in the Method section (namely, including the alumina and graphene layers). (c) Normalized far-field reflection distribution. The two solid lines are for rounded tips at a 12.4 nm gap. Simulations for rounded BT-ant with a 22 nm gap are shown by the dash curve.

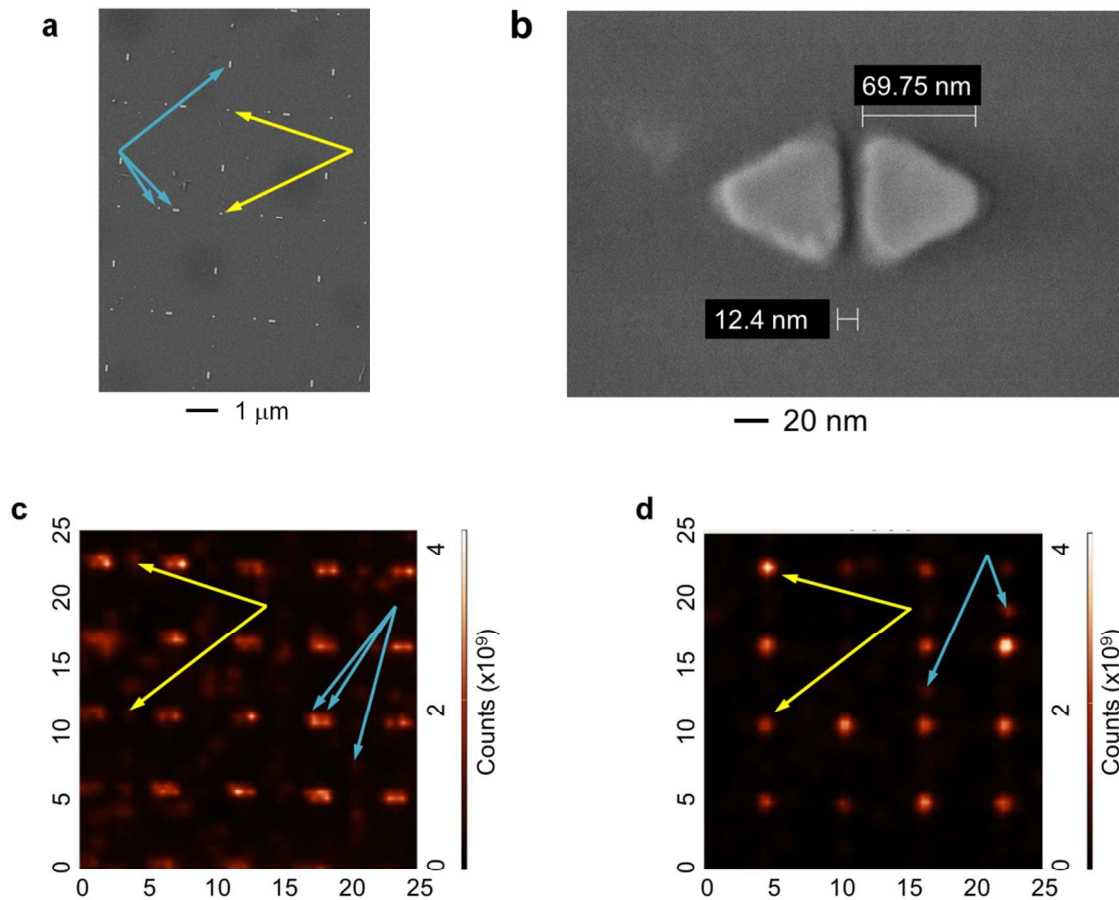


Figure 2: Electronic and optical scattering images. (a) SEM image of the layout: the yellow arrows point to the position of antennas; the light blue arrows point to the position of marks. (b) Diamond-shape optical antenna (D-ant). (c) As-is image for the integrated G-line when the sample was illuminated by a polarized 633 nm HeNe laser. Laser polarization was along the antenna axis (the x-axis). (d) As-is image for the integrated G-line when the sample was illuminated with a 785 nm laser. The laser polarization was along the antenna axis.

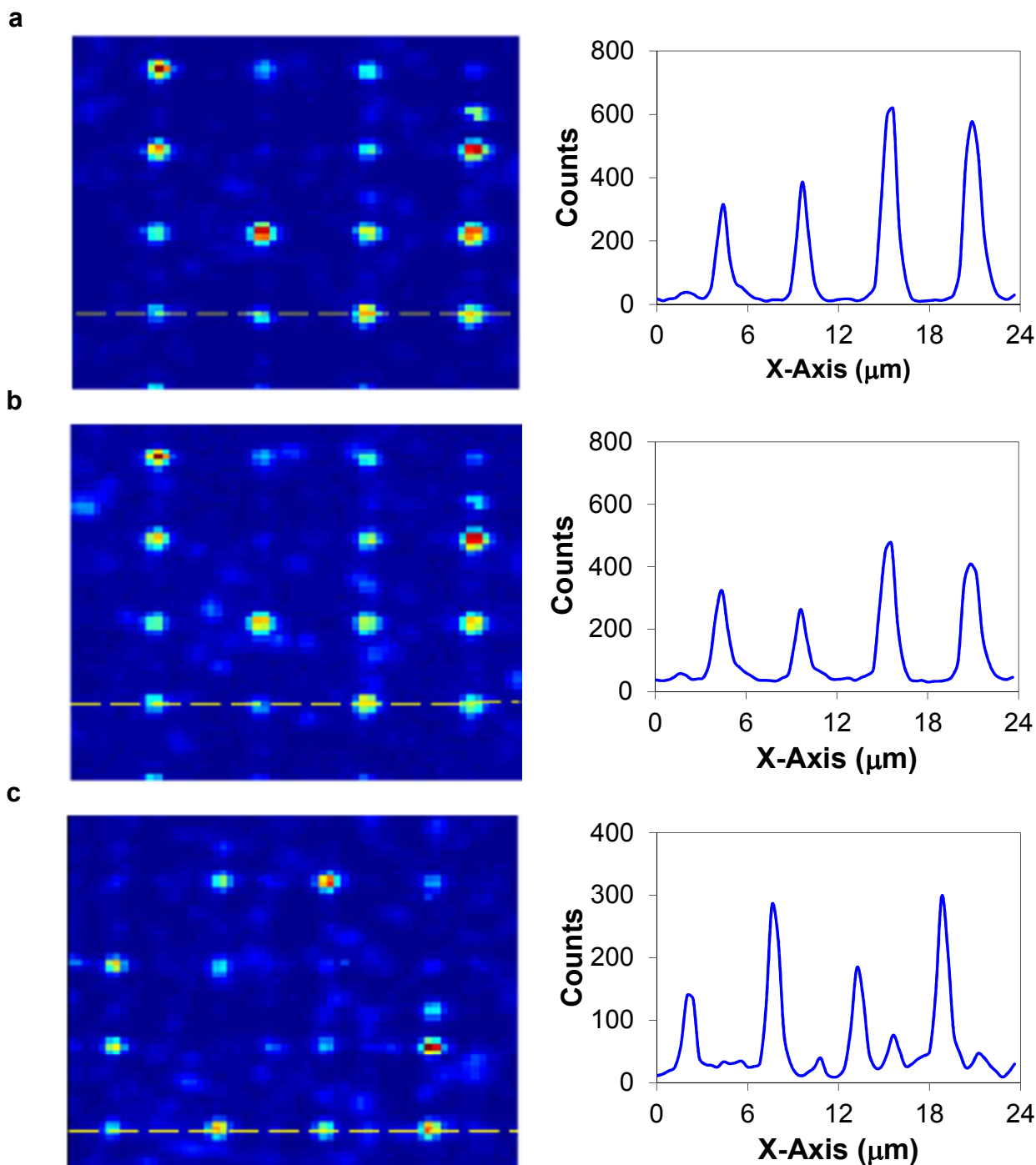


Figure 3: Spatial maps with spectral background corrected. (a) Integrated graphene D-line. (b) Integrated graphene G-line. Both (a), and (b), were taken with laser polarization parallel to the antenna's axis. (c) Integrated graphene D-line taken with laser polarization perpendicular to the antenna's axis. A slight shift of the stage is noted. The antenna's gap of D-ant was nominally 10 nm and the layout was illuminated by a $\lambda=785$ nm laser.

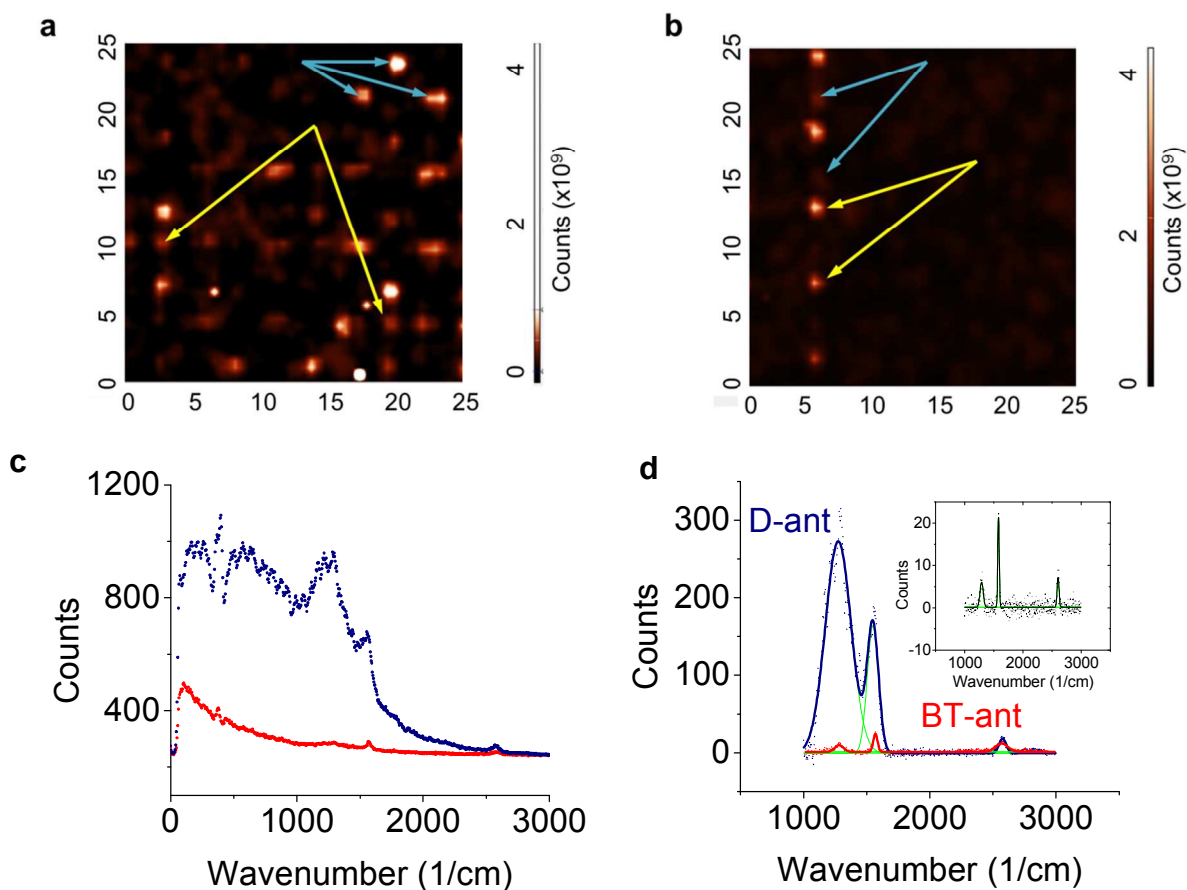


Figure 4: Spatial maps and Raman spectra. (a) As-is spatial maps of graphene 2D line taken with (a) BT-ant and (b) with D-ant. The laser wavelength was 785 nm polarized along the antenna's axis and the antenna's gap was nominally 10 nm. Yellow arrows point to the antennas; light blue arrows point to the fiduciary marks. An optical filter cuts the laser line near zero for both antennas. (c) As-is Raman spectra of both antenna types. (d) Raman spectra. The spectral background was subtracted. The inset shows a typical spectrum of graphene between the D-ant; the relative small amplitude of the 2D-line is due to the limited sensitivity of the Si detector array in this spectral range (~980 nm; see also data for 633 nm laser in the SI section)

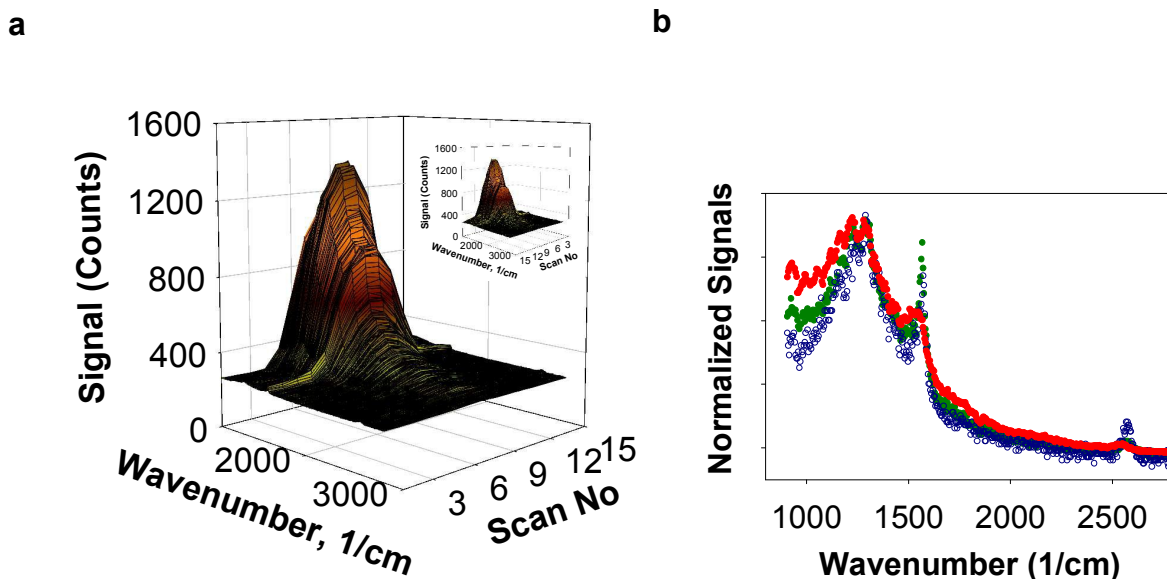


Figure 5. Spatial scans and Raman spectra. (a) Spectral data while the focused laser spot of ca 715 nm was scanning the ca 150 nm D-ant in steps of 200 nm. The spectral range was 1000-3000 cm^{-1} . The laser intensity was maximal, 28.4 mW. The inset exhibits the same data in reverse order. (b) Three raw spectral data of graphene on D-ant: scans 5 (green solid circles), 8 (red solid circles) and 14 (blue open circles). Scan 8 was at maximal power. Scans 5 and 14 were separated by 1.8 μm at 10% of maximal laser power. The signals were normalized to the peak amplitude of the D-line.

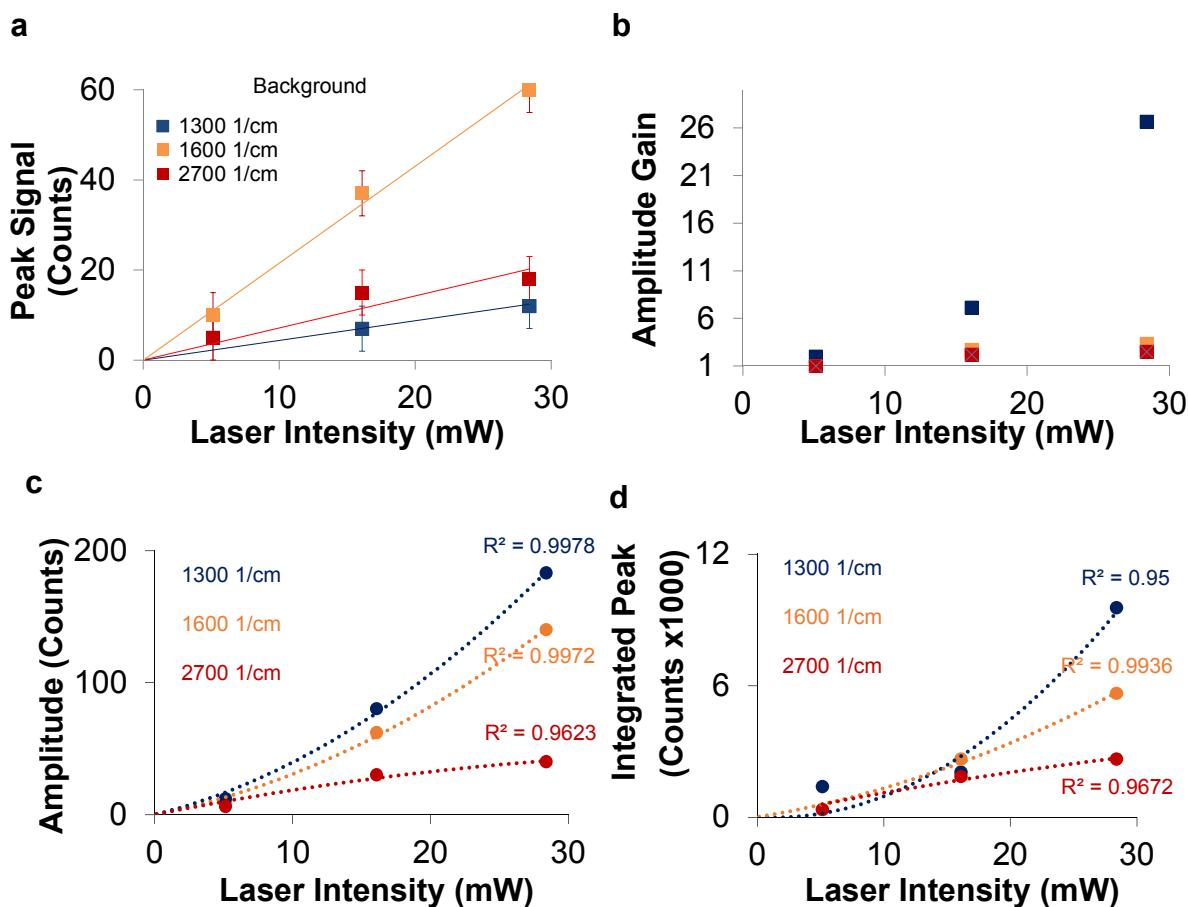


Figure 6. Amplitude and integrated gain. (a) The signal in-between antennas exhibited a linear dependence on the laser intensity (spontaneous Raman scattering). The largest signal comes from the G-line; the largest intensity-dependent effect was obtained for the D-line. (b) Amplitude Gain, defined as the ratio between the signal on the antenna and the signal obtained for area between the antennas, as a function of laser intensity. Alternatively, one may plot the peak amplitude (c) and the integrated peak amplitude (d) as a function of the laser intensity. The set of antennas is different than the one shown in (a), (b).

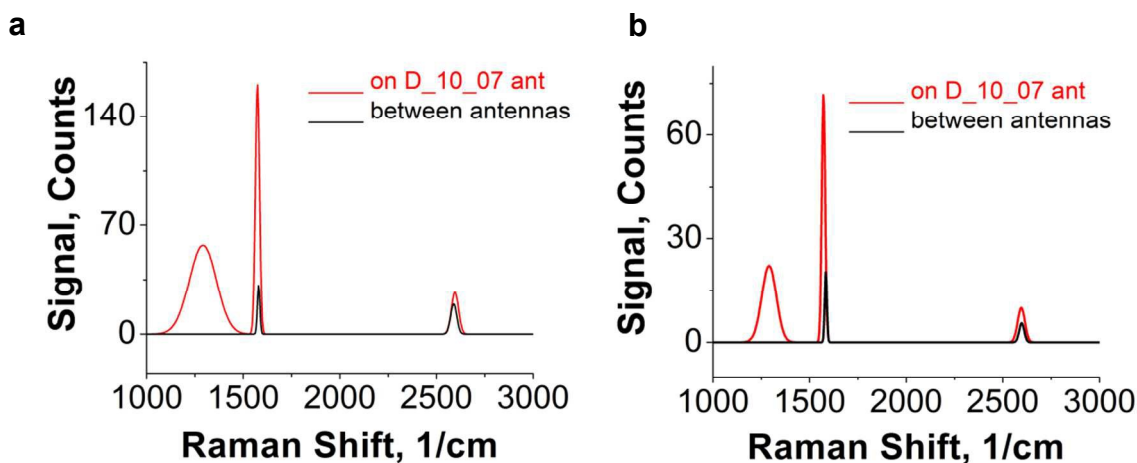


Figure 7. Intensity-dependent spectra. Fitted spectra of D-ant taken at (a) $I_L=16.1$ mW and followed by (b) $I_L=5.14$ mW. The widths of the D-, G- and 2D-lines were, respectively: (a) 140 ± 3 , 21 ± 1 , 36 ± 3 cm^{-1} on the antennas and 12 ± 2 , 31 ± 3.5 cm^{-1} for the area between them (there was no observable D-line). (b) 74 ± 4 , 17 ± 1 , 37 ± 4.5 cm^{-1} on the antennas and 11 ± 2 , 25 ± 2.5 cm^{-1} for the area between them. Upon a decrease of the laser intensity by approximately a factor of 3, the decrease in the integrated peak count was, 5.7, 3 and 5 for the D-, G- and 2D-lines, respectively. The slightly lower 2D line in (b) compared to (a) might be the result of a smaller signal to noise ratio.